PAPER

Check for updates

Dual valence Eu-doped phospho-alumino-silicate glass-ceramics containing Ba₃AlO₃PO₄ nanocrystals for W-LEDs

Xiaoman Li,[ab] Dengke Xu,[a] XueYun Liu[c] and Hai Guo (ID) *[a]

Novel dual valence Eu-doped phospho-alumino-silicate glass-ceramics containing orthorhombic Ba₃AlO₃PO₄ nanocrystals were first fabricated by a traditional melt-quenching method and subsequent heat-treatment in an air atmosphere. Their structural and luminescent properties were systemically investigated by XRD, TEM analysis, and spectroscopic and fluorescence lifetime measurements. The incorporation of Eu^{3+} into Ba₃AlO₃PO₄ crystallites and the reduction mechanism of Eu^{3+} to Eu^{2+} were also discussed based on the optical analyses. Simultaneously, perfect white light emission was obtained under 325 nm excitation. An improved anti-thermal quenching property was achieved resulting from the successful enrichment of Eu^{3+} and Eu^{2+} into Ba₃AlO₃PO₄ crystallites, which was evidenced by active energy calculation. Our results indicate that these dual valence Eu-doped transparent Ba₃AlO₃PO₄ glass-ceramics may have potential applications in W-LEDs.

Introduction

White light-emitting diodes (W-LEDs), the next generation of solid-state light source, have attracted more attention recently due to not only their long lifetime, environment benefits and energy saving but also their wide applications for lighting and displays, such as general illumination, device indicators, backlights, and automobile headlights.[1–5] However, the efficiency of W-LEDs fabricated by ultraviolet (UV) LED chips coupled with tricolor phosphors is limited because of the strong re-absorption of blue light by green and red phosphors.[6–10] Compared to the conventional phosphors used for W-LEDs, white emitting rare earth ion (REI)-doped glass-ceramics not only present excellent luminescent properties and better mechanical properties but also show an epoxy-resin free assembly process[11–20] with a lower production cost and simpler manufacturing procedures. Therefore, it is of urgency to design novel single-phased multi-activator co-doped systems capable of emitting white light under UV chip excitation, which is based on the luminescence and (or) energy transfer between multi-activators.[20–25]

Among the luminescent activators, dual valence europium ions have been widely used in luminescent materials. It is well-known that the emission of Eu^{3+} ion consists of sharp lines in the orange-red spectra region, while that of Eu^{2+} ion is typically broad in the blue-green spectral region.[26–32] Consequently, a perfect white light emission may be achieved in appropriate glass-ceramics by combining the sharp emission of Eu^{3+} and the broad emission of Eu^{2+}.[33,34]

For the glassy host, silicate glasses have attracted considerable interest due to their low-cost, large tensile strength, high chemical durability, and excellent thermal stability. In addition, with the introduction of Al_2O_3, the solubility of REI will be increased and the concentration quenching of luminescence will be limited. Besides, P_2O_5, a kind of glass network modifier, may be conducive to lower viscosity and improve the crystallization process of glass-ceramics.[35] Therefore, highly transparent phospho-alumino-silicate glasses and glass-ceramics are considered as suitable hosts to obtain practically visible luminescence.

Herein, dual valence Eu-doped Ba₃AlO₃PO₄ based phospho-alumino-silicate glass-ceramics were first fabricated by a traditional melt-quenching method in an air atmosphere. Their structure and luminescent properties were systematically investigated. Perfect white light emission and large active energy were achieved under the excitation of UV light, which makes these glass and glass-ceramics good candidates for W-LED phosphors even at high temperatures.

Experimental

The glass samples with nominal composition 35SiO₂–17Al₂O₃–20BaCO₃–20BaF₂–8P₂O₅–0.5EuF₃ (in mol%) were prepared by the melt-quenching method. SiO₂, Al₂O₃, P₂O₅, BaCO₃, BaF₂ (A.R., all from Sinopharm Chemical Reagent Co., Ltd., China), and high purity EuF₃ (99.99%, from AnSheng Inorganic Materials Co., Ltd., China) were used as starting materials. The well-ground

[a] Department of Physics, Zhejiang Normal University, Jinhua, Zhejiang, 321004, China. E-mail: ghh@zjnu.cn

[b] State Key Laboratory of Luminescent Materials and Devices, South China University of Technology, Guangzhou, Guangdong, 510640, China

[c] Laboratory of Infrared Materials and Devices, The Advanced Technology Research Institute, Ningbo University, Ningbo, Zhejiang 315211, China

stoichiometric chemicals were put into a covered alumina crucible and melted at 1500 °C for 1 h in an air atmosphere. The melt was poured onto a 300 °C preheated stainless-steel plate and then pressed by another plate to form the precursor glasses (labeled as PG), followed by annealing at 450 °C for 5 h to release the internal stresses. Subsequently, the PG samples were heat-treated for 2 h at 670 and 680 °C to form the transparent glass-ceramics, which were labeled as GC670 and GC680, respectively. All samples were cut and polished optically with a thickness of 2 mm for further characterization and measurements.

The differential scanning calorimeter (DSC) curve of the PG (powder, 10.0 mg) was collected on a STA449C Jupiter (Netzsch, Germany) apparatus at a heating rate of 10 °C min^{-1} in the range of 40–950 °C in an air atmosphere. X-ray diffraction (XRD) patterns were recorded on a Philips X'Pert PRO SUPER X-ray diffraction apparatus with a Cu Kα radiation. Transmittance spectra were measured on a U-3900 Ultraviolet-Visible (UV-VIS) spectrophotometer (Hitachi). The microstructure of the glass-ceramics was analyzed by a JEM-2010 transmission electron microscope (TEM) (JOEL Ltd., Tokyo, Japan). The excitation, emission spectra, and decay curves were recorded on an Edinburgh FLS920 spectrofluorometer equipped with a continuous wave 450 W Xe lamp, a microsecond flashlamp (μF900), and a nanosecond flashlamp (nF900) as excitation sources. Thermal degradation experiments were also recorded on an Edinburgh FLS920 spectrofluorometer by utilizing a homemade high-temperature unit. All above measurements were carried out at room temperature, except thermal degradation experiments.

Results and discussion

In order to determine the crystallization temperature of this Eu-doped phospho-alumino-silicate glass, the DSC curve of the PG sample was collected at a heating rate of 10 °C min^{-1} in the air atmosphere, as exhibited in Fig. 1(a). An obvious crystallization peak at 755 °C (T_p) with a FWHM (full width at half maximum) of 52.6 °C is observed. The glass transition temperature (T_g) and the onset of crystallization temperature (T_c) are about 630 and 725 °C, respectively. Because of a large difference of 95 °C between T_g and T_c, 670 to 680 °C (40–50 °C beyond T_g) can be used as the crystallization temperature to obtain the glass-ceramics. In this work, 670 and 680 °C were chosen as the heat treatment temperatures for crystallization.

Fig. 1(b) shows the XRD patterns of PG, GC670, and GC680. PG does not exhibit any discrete diffraction peaks, confirming its amorphous nature. Moreover, as shown in the photographic images of the samples (inset in Fig. 1(a)), PG exhibits good transparency. The diffraction peaks of GC670 and GC680 match well with that of orthorhombic $Ba_3AlO_3PO_4$ (JCPDS card no. 45-0059), indicating that the $Ba_3AlO_3PO_4$ based glass-ceramics were elaborated. The size of $Ba_3AlO_3PO_4$ nanocrystals can be estimated by the following Scherrer's equation:[36]

$$D = k\lambda/\beta \cos \theta \quad (1)$$

where $k = 0.89$, $\lambda = 0.154056$ nm represents the wavelength of the Cu Kα radiation, θ is the Bragg angle, and β represents the

corrected half-width of diffraction peak. Here, we used the strongest diffraction peak with $2\theta = 29.3°$, which corresponds to the (222) crystal plane, for calculation. The mean crystalline sizes of $Ba_3AlO_3PO_4$ nanocrystals in GC670 and GC680 are estimated to be about 19 and 21 nm, respectively. Their crystal volume fractions were found to be about 8.5% and 11.1% for GC670 and GC680, respectively, by calculating the ratio of integrating area of the peaks to total integrated area of the XRD patterns. As another sign of the crystallinity, the densities of the samples measured by Archimedes' principle are about 3.70, 3.72, and 3.83 g cm^{-3} for PG, GC670, and GC680, respectively.

The UV-VIS transmittance spectra of PG, GC670, and GC680 in the range of 200–850 nm are shown in Fig. 1(c). The characteristic absorption peaks observed at 393 and 464 nm are ascribed to the transitions from the $^7F_0$ ground state to the $^5L_6$ and $^5D_2$ excited states of Eu^{3+},[34] respectively. The cut-off wavelength of GC gets a red-shift compared to that of PG, which may be attributed to the optical scattering of $Ba_3AlO_3PO_4$ nanocrystals. Similar to PG, the GC samples maintain a perfect transparency (up to 70%) owing to the smaller size of the precipitated $Ba_3AlO_3PO_4$ nanocrystals compared to the wavelength of visible-near infrared (VIS-NIR) light.[34] The transmittance decreases gradually with elevating heat-treatment temperature because of the larger size of nanocrystals and crystallinity after further crystallization, which is reflected in the photographs of the glass samples shown in Fig. 1(a).

The microstructure of the GC680 sample is characterized by TEM and high-resolution TEM (HRTEM) images, as displayed in Fig. 1(d) and (f), respectively. The TEM bright-field micrograph and selected area electron diffraction (SAED) patterns reveal that $Ba_3AlO_3PO_4$ nanocrystals with a polycrystalline diffraction feature are homogeneously dispersed in the amorphous glassy phase. The particle size distribution of $Ba_3AlO_3PO_4$ nanocrystals in the GC680 sample is shown in Fig. 1(e). The results show that the size of $Ba_3AlO_3PO_4$ nanocrystals is at a range of 14–34 nm and the average size is about 21 nm, in accordance with that estimated by the Scherrer's equation. HRTEM image displays the resolved lattice fringes of nano-sized single-crystalline $Ba_3AlO_3PO_4$ clearly and the value of the associated interplanar spacing d is about 0.314 nm, which is corresponding to the (311) crystal plane of orthorhombic $Ba_3AlO_3PO_4$ ($d_{(311)} = 0.313$ nm).

The excitation ($\lambda_{em} = 613$ nm) and emission ($\lambda_{ex} = 393$ nm) spectra of Eu^{3+} ions in the PG and GC samples are given in Fig. 2(a) and (b), respectively. Besides several characteristic sharp peaks assigned to the 4f–4f transitions of Eu^{3+} ions (350–500 nm) from the ground state to the marked excited levels, there is also a broadband at 263 nm originated from the well-known O^{2-}–Eu^{3+} charge-transfer (CT) band in the excitation spectra monitored at the 613 nm emission. The strongest excitation peak at 393 nm corresponds to the $^7F_0 \rightarrow {}^5L_6$ transition of Eu^{3+} (ref. 33 and 34) and the excitation efficiency is apparently intensified for the GC samples compared with that of the PG sample. In the emission spectra excited by 393 nm, the characteristic red emission peaks originating from $^5D_0 \rightarrow {}^7F_J$ ($J = 0$–4) transitions of Eu^{3+} ions (570–720 nm) are detected.[37] The luminescent properties of Eu^{3+} undergo significant changes after crystallization. Compared to those of PG, the red
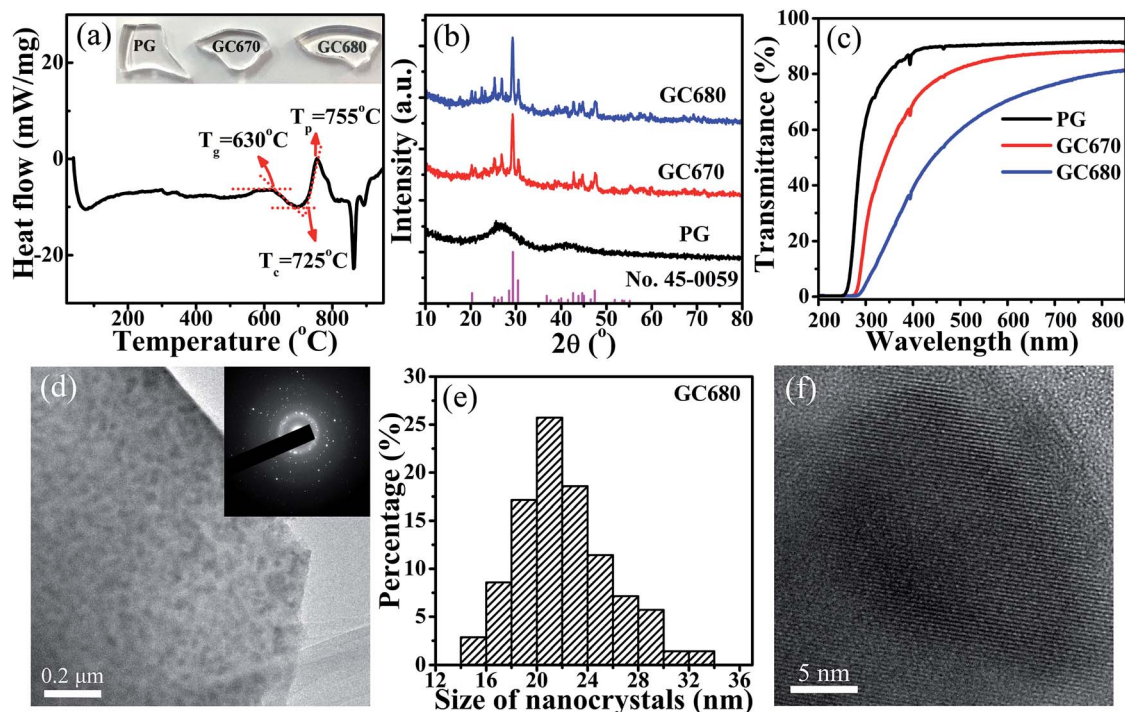
Fig. 1 (a) DSC curve of PG, the inset shows the photographs of PG, GC670, and GC680 samples; (b) XRD patterns of PG, GC670 and GC680, and the reference data of JCPDS card no. 45-0059 for orthorhombic $Ba_3AlO_3PO_4$; (c) transmittance spectra of PG, GC670, and GC680; (d) TEM image of GC680 and the inset is SAED patterns; (e) the size distribution of nanocrystals in GC680; and (f) high-resolution TEM image of GC680.

emissions at 613 and 702 nm of Eu^{3+} ions of GC680 are enhanced by 3 and 6 times, respectively. Stark splitting for $^5D_0 \rightarrow ^7F_2$ transitions of Eu^{3+} ions is also observed after crystallization, as shown in the inset of Fig. 2(b). These phenomena generally confirm the incorporation of Eu^{3+} ions into $Ba_3AlO_3PO_4$ nanocrystals with increasing the symmetrical environment for Eu^{3+}.[34,36] Fig. 2(e) shows the photographs of the PG and GC samples under the excitation of 393 nm light. It can be seen that all glass samples emit red light.

It is well-known that $^5D_0 \rightarrow ^7F_2$ electric dipole transition of Eu^{3+} is forbidden in the centrosymmetric environment, while $^5D_0 \rightarrow ^7F_1$ magnetic dipole transition does not depend on the symmetry of the environment that Eu^{3+} is located in. As a result, the intensity ratio R of $^5D_0 \rightarrow ^7F_2$ to $^5D_0 \rightarrow ^7F_1$ emissions can be taken as a spectral probe to detect the symmetry of local crystal field that Eu^{3+} is located in. A lower value of R suggests a higher crystal symmetry.[13-15] In this work, the integrated intensity ratios R calculated are 3.3, 2.5, and 2.4 for PG, GC670, and GC680, respectively. Hence, the decrease of the R value after heat-treatment is another evidence for the incorporation of Eu^{3+} into the symmetric environment of $Ba_3AlO_3PO_4$ nanocrystals.

The fluorescence decay curves of Eu^{3+} emission can further evaluate the surroundings that Eu^{3+} is located in. Fig. 3(a) shows the decay curves of the 613 nm ($^5D_0 \rightarrow ^7F_2$ transition) emission of Eu^{3+} ions (λ_{ex} = 393 nm) in the PG and GC samples. For all samples, the observed decay curves approximately follow a single exponential function. The lifetimes of PG, GC670, and GC680 are about 2.25, 2.56, and 2.63 ms, respectively. Slightly longer lifetimes for the glass-ceramics indicate that Eu^{3+} ions

are partially incorporated into the $Ba_3AlO_3PO_4$ crystalline phase.

Briefly summarized, the increased luminescence intensities of Eu^{3+} ions, the obvious Stark splitting, the decreased intensity ratio R, and the longer fluorescence lifetimes of the GC samples indicate that Eu^{3+} ions have been partially incorporated into $Ba_3AlO_3PO_4$ nanocrystals after crystallization. Such phenomena may be attributed to the smaller ion radii of Eu^{3+} (0.0947 nm) compared to that of Ba^{2+} (0.1350 nm).[38]

Noteworthy, besides the sharp emissions of Eu^{3+}, a pronounced broad emission centered at about 450 nm from Eu^{2+} is also detected, implying that a part of Eu^{3+} ions is reduced to Eu^{2+} in the present host. The Eu^{2+}-related characteristic excitation (λ_{em} = 450 nm) and emission (λ_{ex} = 325 nm) spectra in PG, GC670, and GC680 are presented in Fig. 2(c) and (d), respectively. The excitation band at 270–390 nm is ascribed to the $4f^7 \rightarrow 4f^65d$ transition of Eu^{2+}. The intense broad emission band in the range of 390–560 nm is due to the $4f^65d \rightarrow 4f^7$ transition of Eu^{2+}.[33,34] For PG, the emission intensity of Eu^{2+} is very weak, implying that only small quantity of Eu^{3+} is reduced to Eu^{2+}. After crystallization, the intensity of the Eu^{2+} emission is enhanced remarkably with increasing the crystallization temperature, which reveals that more Eu^{3+} ions are reduced to Eu^{2+} ions during the crystallization process. The resultant Eu^{2+} (0.1170 nm)[38] ions undergo more ordered local crystal field environments with the incorporation into $Ba_3AlO_3PO_4$ nanocrystals by displacing the positions of Ba^{2+},[39] reflected by the narrowed full width of half maximum (FWHM) of 63 nm in GC670 (or GC680) compared to 77 nm in PG. Fig. 2(f) presents
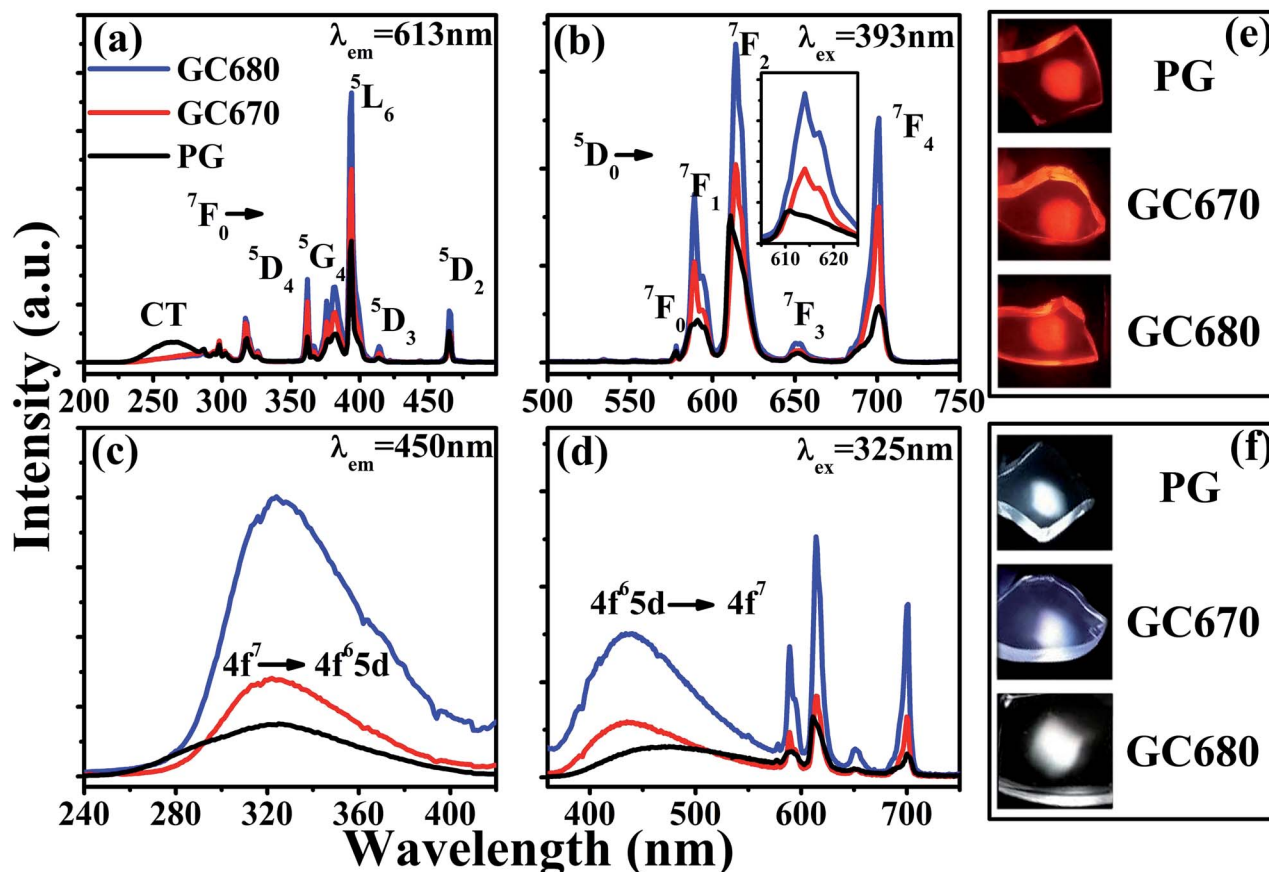
Fig. 2 (a) Excitation spectra (λ_{em} = 613 nm) and (b) emission spectra (λ_{ex} = 393 nm) of Eu^{3+} of the PG and GC samples; (c) excitation spectra (λ_{em} = 450 nm) and (d) emission spectra (λ_{ex} = 325 nm) of Eu^{2+} of the PG and GC samples; the photographs of the samples under the excitation of (e) 393 and (f) 325 nm light.

the glass photographs under 325 nm radiation. Intriguingly, the emitting light colors of the glass samples vary from greenish-white in PG to bluish-white and then to perfect white in GC670 and GC680, respectively.

The fluorescence decay curves of Eu^{2+} (λ_{ex} = 325 nm and λ_{em} = 450 nm), as shown in Fig. 3(b), can further illustrate the above

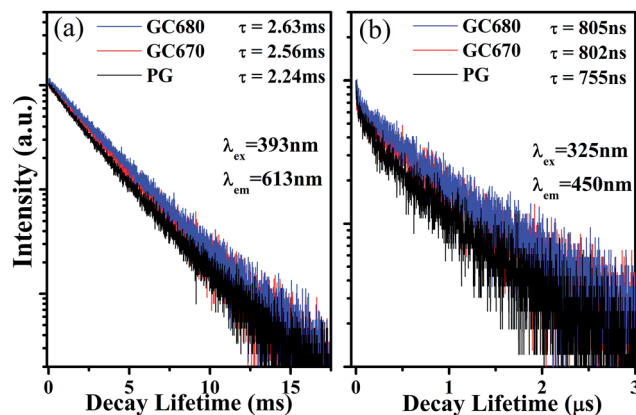**Fig. 3** Luminescent decay curves of (a) $^5D_0 \rightarrow {}^7F_2$ transition (613 nm) of Eu^{3+} (λ_{ex} = 393 nm), and (b) $4f^65d \rightarrow 4f^7$ transition (450 nm) of Eu^{2+} (λ_{ex} = 325 nm).

point. Decay curves of Eu^{2+} emission in all glass samples do not follow the single exponential decay equation, but a double exponential decay equation with a shorter and a longer lifetime components. Hence, here, the lifetimes of Eu^{2+} ions are characterized uniformly by the average lifetime ($\bar{\tau}$) derived by:[21]

$$\bar{\tau} = \int tI(t)\mathrm{d}t \bigg/ \int I(t)\mathrm{d}t \qquad (2)$$

where $I(t)$ stands for the intensity at time t. The average lifetimes $\bar{\tau}$ are 755, 802, and 805 ns for PG, GC670, and GC680, respectively. The longer lifetime of Eu^{2+} in the GC samples strongly proves the partial incorporation of Eu^{2+} into orthorhombic $Ba_3AlO_3PO_4$ nanocrystals.

The reduction mechanism of Eu^{3+} to Eu^{2+} in the air atmosphere can be illustrated perfectly by a charge compensation model.[28,40] When doped into $Ba_3AlO_3PO_4$ nanocrystals, Eu^{3+} will replace Ba^{2+} ions. Meanwhile, two Eu^{3+} ions are needed to substitute three Ba^{2+} ions to maintain the charge balance. Consequently, one cation vacancy $[V''_{Ba}]$ and two defects $[Eu^{\cdot}_{Ba}]$ would be created simultaneously. Here, V''_{Ba} holds two negative charges, while $Eu^{\cdot}_{Ba}$ bears one positive charge. V''_{Ba} acts as an electron donor, while $Eu^{\cdot}_{Ba}$ becomes an electron acceptor. By continuous thermal stimulation, the electrons in vacancy defect V''_{Ba} are released and then trapped by $Eu^{\cdot}_{Ba}$, reducing Eu^{3+} ions

to Eu^{2+} ions. As a result, Eu^{3+} ions are efficiently reduced to Eu^{2+} ions within the precipitated Ba$_3$AlO$_3$PO$_4$ nanocrystals in the glass-ceramics.

Due to the great difference in the excitation spectrum characteristics of Eu^{2+} and Eu^{3+}, a tunable visible emission ranging from blue to red can be achieved by simply altering the excitation wavelength. Fig. 4(a) presents the Commission International de I'Eclairage (CIE) chromaticity coordinates of the PG and GC680 samples excited by 320–375 nm. Both PG and GC680 samples exhibit a tunable luminescent color, covering green-white, blue-white light to warm-white and then red light. It needs to be mentioned that good white light emissions can be achieved in the PG, GC670, and GC680 samples excited by 325 nm UV light, which was exhibited in Fig. 2(f). And the related CIE chromaticity coordinates of the PG and GC samples are shown in Fig. 4(b). Obviously, the CIE chromaticity coordinates of all samples are in the white region and close to the standard equal energy white light illuminate ($X = 0.333$, $Y = 0.333$). The emitting light color of the glass sample can be tuned from green-white light in PG to red-white light in the GC samples after crystallization, which suggests that the mixed-valence Eu-doped Ba$_3$AlO$_3$PO$_4$ glass-ceramics can act as white-emitting phosphors for UV LED chips.

In practical applications, the thermal quenching property is an important technological parameter for a luminescent glass in the solid-state lighting field because it greatly affects the color rendering index and the light output of LEDs,[41–43] which will finally determine whether glass phosphors can sustain a long-term emission efficiency at temperatures over 423 K in LED. Therefore, it is necessary to evaluate the thermal quenching property of the glass particularly at temperatures higher than room temperatures. In order to ensure the results as accurate as possible, 330 nm was chosen as the most effective excitation wavelength for these dual valence europium doped glass and glass-ceramics. Fig. 5(a) and (b) show the emission spectra of the PG and GC680 sample excited by 330 nm at different temperatures, respectively. The insets in the figures are the partially enlarged view of Eu^{2+} emission. Clearly, both emission intensities of Eu^{2+} and Eu^{3+} decrease with increasing temperature. The intensities of Eu^{2+} and Eu^{3+} in GC680 at 423 K remain about 79% and 55% of the initial intensity at 303 K, respectively.

Generally, the thermal quenching with increasing temperature is caused by the enhancement of thermally active multi-phonon nonradiative rate from the luminescent state to a lower state. The thermally activated nonradiative transition rate k_{nr} is given by:[44,45]

$$k_{nr} = s \exp(-\Delta E_a / k_B T) \qquad (3)$$

where s is the frequency factor, ΔE_a is the activation energy, k_B is the Boltzmann constant (8.629×10^{-5} eV K^{-1}), and T is the temperature in Kelvin. A higher activation energy leads to a lower nonradiative rate. The value of the activation energy ΔE_a can be evaluated from the temperature-dependent luminescence spectra by the modified Arrhenius equation:[43,46]
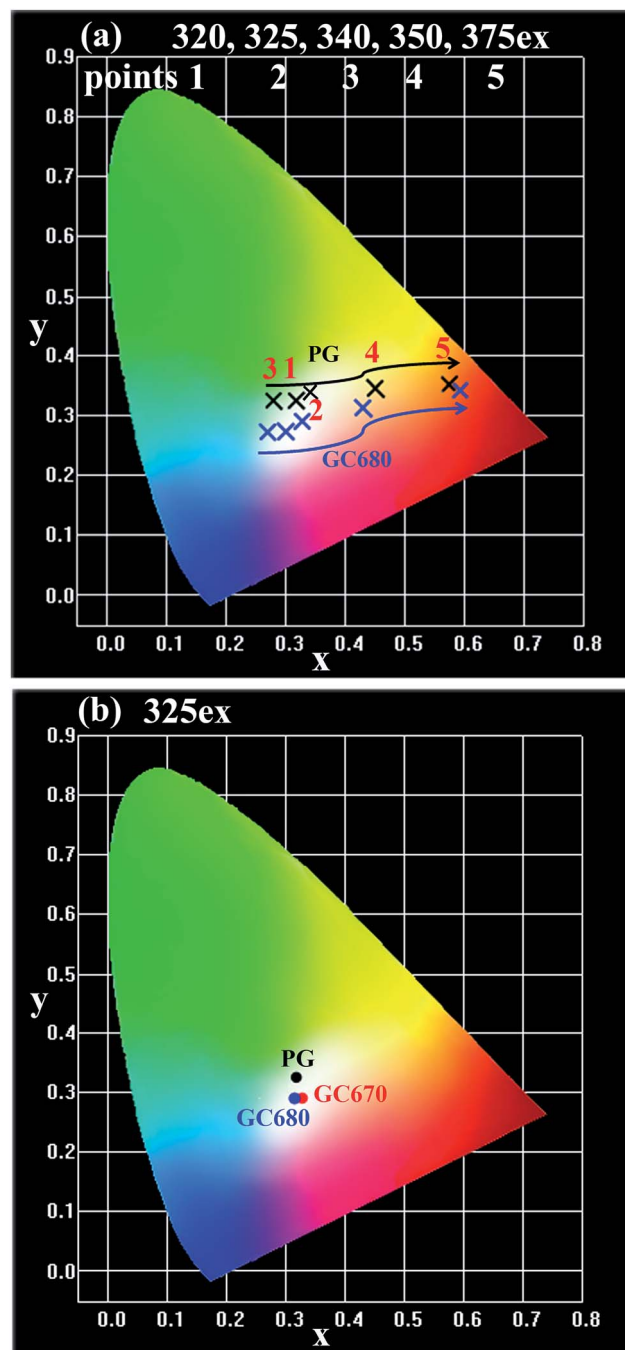

Fig. 4 CIE chromaticity coordinates of (a) PG and GC680 under different excitations (λ_{ex} = 320, 325, 340, 350, and 375 nm, corresponding to points 1 to 5, respectively) and (b) PG, GC670, and GC680 excited by 325 nm.

$$I_T = \frac{I_0}{1 + C \exp(-\Delta E_a / k_B T)} \qquad (4)$$

where I_0 is the initial emission intensity (at 303 K), I_T is the integral emission intensity at different temperatures T, and C is a constant. The temperature-dependent emission intensities of Eu^{2+}, Eu^{3+}, and the overall emission in PG and GC680 are fitted into the above equation, which is shown in Fig. 5(c) and (d),

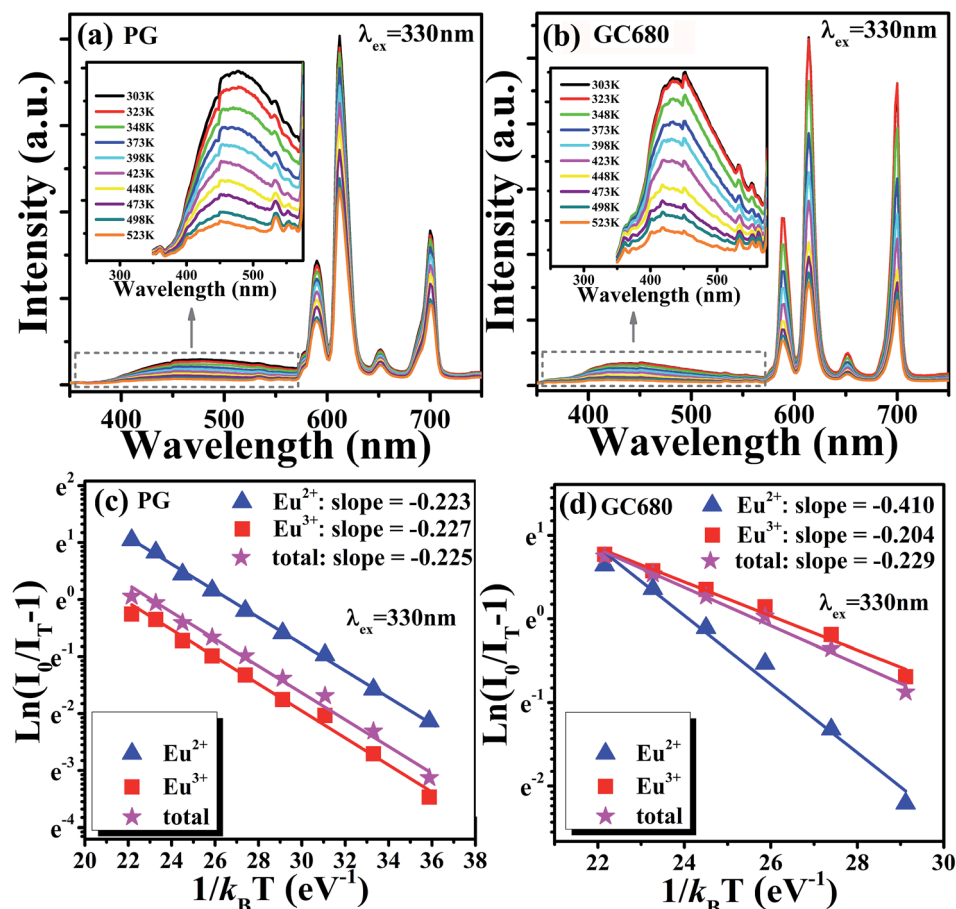**Fig. 5** Temperature-dependent emission spectra ($\lambda_{ex} = 330$ nm) of (a) PG and (b) GC680 samples, the inset is the corresponding partial enlarged view of Eu^{2+} emission spectra; plot of ln($I_0/I_T - 1$) v.s. $1/k_BT$, and the linear fit of the data through eqn (4) of (c) PG and (d) GC680.

respectively. The plot of $\ln(I_0/I_T - 1)$ vs. $1/k_BT$ yields a straight line whose slope determines the activation energy ΔE_a. The values of ΔE_a for Eu^{2+} and Eu^{3+} in PG are calculated to be about 0.223 and 0.227 eV, respectively, implying a slightly rapid degradation for the emission of Eu^{2+} in comparison with that of Eu^{3+}. Those in GC680 are about 0.410 and 0.204 eV, respectively. The visibly larger value of ΔE_a for Eu^{2+} than Eu^{3+} suggests a better anti-thermal quenching property of Eu^{2+} after crystallization once Eu^{2+} ions are incorporated into Ba$_3$AlO$_3$PO$_4$ nanocrystals. The better thermal stability may be due to the smaller difference of ion radius between Eu^{2+} (0.1170 nm) and Ba^{2+} (0.1350 nm),[38] as well as their same valence state. As for the whole emission spectra in PG and GC680, their activation energies are also obtained from the fitting slopes of 0.225 and 0.229 eV, respectively.

The slightly larger value of ΔE_a in GC680 implies better anti-thermal degradation property of GC680 than that of PG. This result indicates that our glass-ceramics have a better thermal stability than PG, which makes the glass-ceramics promising as phosphors for W-LEDs in practice.

Conclusions

Highly transparent dual valence Eu-doped orthorhombic Ba$_3$-AlO$_3$PO$_4$ based glass-ceramics were first fabricated by a melt-

quenching method. The luminescent properties of Eu^{3+} and Eu^{2+} ions in the precursor glass and glass-ceramics revealed the incorporation of Eu^{3+} and Eu^{2+} ions into the Ba$_3$AlO$_3$PO$_4$ crystalline phase by displacing Ba^{2+} lattice sites after crystallization. By combining the sharp orange-red emission of Eu^{3+} and the broad blue-green emission of Eu^{2+}, perfect white light emissions can be achieved by the excitation of 325 nm UV light. A larger active energy of Eu^{2+} than Eu^{3+} after crystallization further manifests the incorporation of Eu^{2+} into Ba$_3$AlO$_3$PO$_4$ nanocrystals with a better anti-thermal quenching property. All results indicate that such dual valence Eu-doped transparent Ba$_3$AlO$_3$PO$_4$ glass and glass-ceramics can be considered as good candidates for phosphor in W-LEDs.

Conflicts of interest

There are no conflicts to declare.

Acknowledgements

Notes and references

1 E. F. Schubert and J. K. Kim, *Science*, 2005, **308**, 1274–1278.

2 P. F. Smet, A. B. Parmentier and D. Poelman, *J. Electrochem. Soc.*, 2011, **158**, R37–R54.

3 D. Chen, Y. Yu, H. Lin, P. Huang, F. Weng, Z. Shan and Y. Wang, *Opt. Lett.*, 2009, **34**, 2882–2884.

4 B. Zhu, S. Zhang, S. Zhou, N. Jiang and J. Qiu, *Opt. Lett.*, 2007, **32**, 653–655.

5 D. Ramachari, L. R. Moorthy and C. K. Jayasankar, *Ceram. Int.*, 2014, **40**, 11115–11121.

6 Y. Narukawa, I. Niki, K. Izuno, M. Yamada, Y. Murazaki and T. Mukai, *Jpn. J. Appl. Phys., Part 2*, 2002, **41**, L371–L373.

7 X. Piao, T. Horikawa, H. Hanzawa and K. I. MacHida, *Appl. Phys. Lett.*, 2006, **88**, 161908.

8 F. W. Kang, H. S. Zhang, L. Wondraczek, X. B. Yang, Y. Zhang, D. Y. Lei and M. Y. Peng, *Chem. Mater.*, 2016, **28**, 2692–2703.

9 F. W. Kang, M. Y. Peng, D. Y. Lei and Q. Y. Zhang, *Chem. Mater.*, 2016, **28**, 7807–7815.

10 M. Y. Peng, X. W. Yin, P. A. Tanner, M. G. Brik and P. F. Li, *Chem. Mater.*, 2015, **27**, 2938–2945.

11 S. Yi, W. J. Chung and J. Heo, *J. Am. Ceram. Soc.*, 2014, **97**, 342–345.

12 R. Zhang, H. Lin, Y. Yu, D. Chen, J. Xu and Y. Wang, *Laser Photonics Rev.*, 2014, **8**, 158–164.

13 G. Gao, N. Da, S. Reibstein and L. Wondraczek, *Opt. Express*, 2010, **18**, A575–A583.

14 G. Gao, S. Reibstein, M. Peng and L. Wondraczek, *J. Mater. Chem.*, 2011, **21**, 3156–3161.

15 G. Gao and L. Wondraczek, *Opt. Mater. Express*, 2014, **4**, 476–485.

16 D. Chen, Y. Yu, P. Huang, H. Lin, Z. Shan and Y. Wang, *Acta Mater.*, 2010, **58**, 3035–3041.

17 Q. Luo, X. Qiao, X. Fan, H. Yang, X. Zhang, S. Cui, L. Wang and G. Wang, *J. Appl. Phys.*, 2009, **105**, 043506.

18 Z. Lin, X. Liang, Y. Ou, C. Fan, S. Yuan, H. Zeng and G. Chen, *J. Alloys Compd.*, 2010, **496**, L33–L37.

19 H. Guo, F. Li, R. Wei, H. Zhang and C. Ma, *J. Am. Ceram. Soc.*, 2012, **95**, 1178–1181.

20 X. M. Li, J. K. Cao, F. F. Hu, R. F. Wei and H. Guo, *RSC Adv.*, 2017, **7**, 35147–35153.

21 H. Guo, R. F. Wei and X. Y. Liu, *Opt. Lett.*, 2012, **37**, 1670–1672.

22 H. Guo, X. Wang, J. Chen and F. Li, *Opt. Express*, 2010, **18**, 18900–18905.

23 H. Zeng, Z. Lin, Q. Zhang, D. Chen, X. Liang, Y. Xu and G. Chen, *Mater. Res. Bull.*, 2011, **46**, 319–322.

24 H. Lin, D. Chen, Y. Yu, A. Yang, R. Zhang and Y. Wang, *Mater. Res. Bull.*, 2012, **47**, 469–472.

25 M. L. C. Jota, A. G. Murillo, F. C. Romo, M. G. Hernandez, A. D. M. Ramirez, S. Velumani, E. D. Cruz and A. Kassiba, *Mater. Res. Bull.*, 2014, **51**, 418–425.

26 S. Liu, G. Zhao, W. Ruan, Z. Yao, T. Xie, J. Jin, H. Ying, J. Wang and G. Han, *J. Am. Ceram. Soc.*, 2008, **91**, 2740–2742.

27 C. Zhu, Y. Yang, X. Liang, S. Yuan and G. Chen, *J. Am. Ceram. Soc.*, 2007, **90**, 2984–2986.

28 S. Taruta, M. Matsuki, H. Nishikiori, T. Yamakami, T. Yamaguchi and K. Kitajima, *Ceram. Int.*, 2010, **36**, 1303–1309.

29 G. J. Gao, J. X. Wei, Y. Shen, M. Y. Peng and L. Wondraczek, *J. Mater. Chem. C*, 2014, **2**, 8678–8682.

30 G. J. Gao and L. Wondraczek, *J. Mater. Chem. C*, 2014, **2**, 691–695.

31 M. Chowdhury and S. K. Sharma, *RSC Adv.*, 2015, **5**, 51102–51109.

32 A. A. Reddy, S. Das, S. Ahmad, S. S. Babu, J. M. F. Ferreira and G. V. Prakash, *RSC Adv.*, 2012, **2**, 8768–8776.

33 H. Guo, X. Liu, F. Li, R. Wei, Y. Wei and C. Ma, *J. Electrochem. Soc.*, 2012, **159**, J223–J226.

34 X. Liu, Y. Wei and H. Guo, *J. Am. Ceram. Soc.*, 2013, **96**, 369–371.

35 F. Fu, B. Chen, L. Shen, E. Y. B. Pun and H. Lin, *J. Alloys Compd.*, 2014, **582**, 265–272.

36 X. Liu, Y. Wei, R. Wei, J. Yang and H. Guo, *J. Am. Ceram. Soc.*, 2013, **96**, 798–800.

37 C. Zhang, S. Zhao, D. Deng, L. Huang, Y. Tian and S. Xu, *Ceram. Int.*, 2014, **40**, 2737–2740.

38 R. D. Shannon, *Acta Crystallogr., Sect. A: Cryst. Phys., Diffr., Theor. Gen. Crystallogr.*, 1976, **32**, 751–767.

39 Q. Luo, X. Fan, X. Qiao, H. Yang, M. Wang and X. Zhang, *J. Am. Ceram. Soc.*, 2009, **92**, 942–944.

40 M. Peng, Z. Pei, G. Hong and Q. Su, *J. Mater. Chem.*, 2003, **13**, 1202–1205.

41 Z. G. Xia, Z. H. Xu, M. Y. Chen and Q. L. Liu, *Dalton Trans.*, 2016, **45**, 11214–11232.

42 X. J. Zhang, L. Huang, F. J. Pan, M. M. Wu, J. Wang, Y. Chen and Q. Su, *ACS Appl. Mater. Interfaces*, 2014, **6**, 2709–2717.

43 X. Y. Liu, H. Guo, S. X. Dai, M. Y. Peng and Q. Y. Zhang, *Opt. Mater. Express*, 2016, **6**, 3574–3585.

44 S. Saha, S. Das, U. K. Ghorai, N. Mazumder, D. Ganguly and K. K. Chattopadhyay, *J. Phys. Chem. C*, 2015, **119**, 16824–16835.

45 J. H. Li, J. Yan, D. W. Wen, W. U. Khan, J. X. Shi, M. M. Wu, Q. Su and P. A. Tanner, *J. Mater. Chem. C*, 2016, **4**, 8611–8623.

46 K. J. Laidler, *J. Chem. Educ.*, 1984, **61**, 494.